Publ. Natl. Astron. Obs. Japan Vol. 10. 1 – 14 (2007)

The Fiber Multi-Object Spectrograph for the Okayama 188cm Telescope – Development and Observation –

Hiroyuki MITO[1],
Yoshikazu NAKADA[1], Hiroshi KAROJI[2], Junichi NOUMARU[3],
Kiichi OKITA[4], Yuji NORIMOTO[4], Tomohiko OZAWA[5], Yasushi YADOUMARU[5], Nobunari ITOH[6],
Akito TAJITSU[3], Takao SOYANO[1], Ken-ichi TARUSAWA[1]
mitohr@cc.nao.ac.jp
(Received 2007 March 20; Accepted 2007 Aug 6)

Abstract

A fiber multi-object spectrograph for the Okayama 188cm telescope (OFMS) has been developed. We found two problems at the observation in 1993. The first was that the spectra were low quality without sufficient photon counts due to smaller efficiency than expected. The second was the complicated procedure in operating the OFMS. We have solved these problems with the development started in 1993. Currently, the OFMS is capable of observing 30 celestial objects simultaneously in a field of view of 1 degree. The resolution of the spectrograph is $\lambda/\Delta\lambda = 100 - 150$. It is possible to observe spectra of S/N=100 for a mv=10 star at a 1.25 minutes exposure. In April and May 1999, we observed four open clusters and determined the metallicity [Fe/H] for each. We recorded four metallicities as; +0.15 dex for NGC6709, +0.09 dex for IC4665, –0.36 dex for NGC6866, and +0.07dex for NGC6633.

keywords: fiber multi-object spectrograph–open cluster–metallicity

1. Introduction

The fiber multi-object spectrograph (FMS) simultaneously captures multiple spectra of stars or galaxies on a telescope focal plane. The development of FMS started in the 1970's by evaluating the capability of an optical fiber for astronomical observation. The first FMS was the so-called MEDUSA. It observed 8 galaxies in the Abell 754 cluster of galaxies in 1979 (Hill et al. 1980, Hill 1988). Since then, many FMSs have been developed, such as ARGUS, Autofib, FLARE, 2dF, 6dF, FMOS, OzPoz and so forth. Currently, we use FMSs in several observatories, and many observational projects have been making remarkable progress.

The development of the fiber multi-object spectrograph for the Okayama 188cm telescope (OFMS) was started in 1990 by the OFMS development team at the National Astronomical Observatory Japan. The basic design and evaluation for the instrument are reported in the paper (Noumaru, et. al. (1993)). The instrument was developed for the purpose of observing clusters of galaxies, young stellar objects (open clusters, star forming regions) and others. However, several subsequent test observations showed the difficulty of achieving expected performances. The instrument mainly showed two problems. The first was that the spectra were low quality without sufficient photon counts due to smaller efficiency than expected. The second was that the complicated procedures to operate the instrument reduced the total observational efficiency.

In this paper, we show the development required to complete the OFMS, and the observational results obtained by using it. In section 2, we describe the study which has been done to solve the problems of the OFMS. Additionally, we describe the spectrograph which has been used in observations since 1995. The performance of the OFMS is summarized in section 3. We observed 4 open clusters with the OFMS to measure the metallicity [Fe/H] for each of them. In section 4, we explain the observation and the methods which were used to determine their metallicity [Fe/H]. A summary and conclusion are described in section 5. This paper is a partial fulfillment of Mito's doctoral dissertation (Mito 2000).

[1] Kiso observatory, Institute of Astronomy, School of Science, The University of Tokyo, Kiso, Nagano, 397-0101, Japan
[2] National Astronomical Observatory of Japan, Mitaka, Tokyo, 181-8588, Japan
[3] National Astronomical Observatory of Japan, Hawaii, USA
[4] National Astronomical Observatory of Japan, Okayama, Japan
[5] Misato Observatory, Kimino, Wakayama, Japan
[6] Mie University, Tsu, Mie, Japan

2. Instrument Refurbishment

The OFMS is composed of a fiber positioner, a spectrograph mounted on a Cassegrain focus and optical fibers connecting them. Figure 1 shows the schema of the OFMS and the Okayama 188cm telescope. Before the refurbishment started in 1993, we used the Okayama Cassegrain Spectrograph as the spectrograph in the OFMS. Since 1993, it has been replaced with the new spectrograph which was designed for spectroscopy using optical fibers. The details will be mentioned in section 2.3. The fiber positioner is attached to a Newtonian focus (F/5). It sets the fibers to astronomical object image positions on the focal plane. The received photons are carried through the optical fibers and arrive at the spectrograph slit. Figure 2 shows a schema of the focal plane device. There is a manipulator unit in the focal plane device, which is mounted on the XYZ stages. The manipulator picks up the fibers and places them in position on the astronomical object image.

In the case of the refurbished OFMS, we replaced the Z coordinate motor of the XYZ stages. The new Z motor is equipped with a rotary encoder, this allows us to control the fiber position precisely. In addition, some parts of the manipulator have been rebuilt or replaced to solve directly or indirectly the problem of reducing the light power from the telescope. In the first subsection (2.1), we will show the solutions for four most serious problems; (*i*) defocusing of the optics to detect fiber probes, (*ii*) the position error for measuring a fiber probe by the optics, (*iii*) the design error of the fiber probes to adjust telescope focus and (*iv*) unexpected behavior of optical fibers and the electromagnetic manipulator.

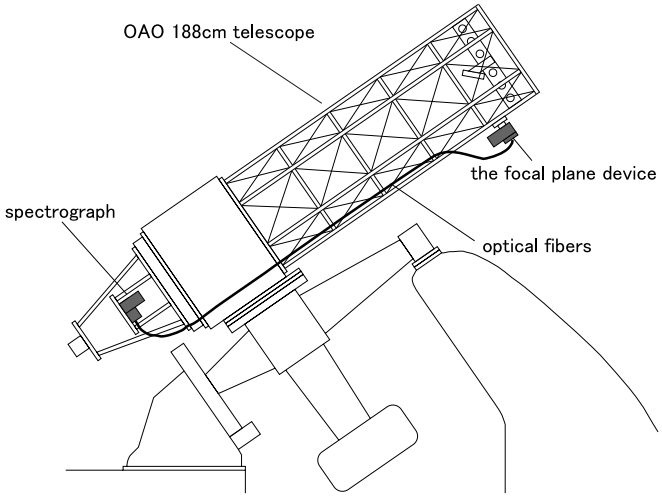

Figure 1. The fiber multi-object spectrograph for the Okayama 188cm telescope (OFMS).

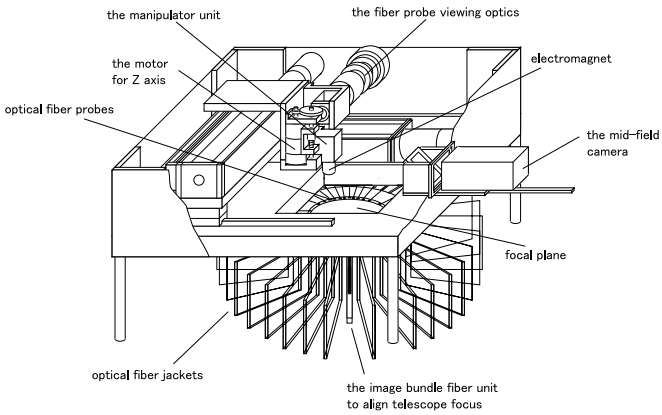

Figure 2. The focal plane device of OFMS.

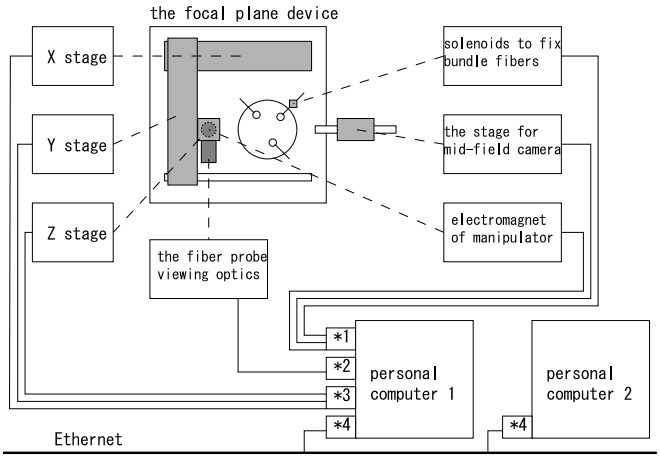

Figure 3. Operating system of the instrument (*1 parallel I/O board, *2 RS232C board, *3 stage controller board, *4 Ethernet adapter).

Figure 3 shows the OFMS operating system. There are 2 personal computers (PC1 and PC2) in the system. PC1 controls all devices of the OFMS through the interface boards, and PC2 serves as the user interface. Both computers are connected with Ethernet. In the previous system, the fiber probe viewing optics was controlled by another independent personal computer. The activation of the Z coordinate and the control of the mechanical devices shown in figure 3 were operated by an independent CPU unit. A new operating system allowed us to execute a highly integrated command to control the OFMS automatically. This reduced the preparation time required for the observation. We show details of this control system in the second subsection (2.2).

2.1. the Optics of the Focal Environment Assembly

We researched the factors which are required to obtain sufficient photon counts. As a result, we found three improvement factors in the optics of the focal environment assembly.

2.1.1. *Focusing Position of the Fiber Probe Viewing Optics*

The fiber probe viewing optics is installed in the manipulator head. The optics can move anywhere on the field plate and measure both the positions of astronomical objects and fiber probes. The schematic optical arrangement is shown in figure 4. The basic design is shown in the optics planned for the William Herschel Telescope (Parry and Lewis(1990)). The optics is composed of a cube beam splitter, a convex lens and a retro reflector. The cube beam splitter has a mirror-coating layer. The layer is divided into two regions; one region has a low reflecting ratio coating and the other a high reflecting ratio coating. The center region acts as a beam splitter, and the outer region acts as a mirror. The light from an astronomical object enters the top surface of the cube beam splitter. Since the cross section of the beam of light is in the shape of a ring, the light enters only the outer region of the mirror-coating layer and is reflected to the CCD imager (see right side figure 4). In contrast, light from a probe enters the bottom surface through the narrow hole penetrating the electromagnetic manipulator and illuminates the center part of the layer. In this case, the light is generated by the other end face of the fiber probe on the spectrograph part being illuminated by a high-luminance LED. As the layer acts as a beam splitter in this region, part of the light is reflected to the lens and the retro reflector (see left side figure 4) and arrives at the CCD imager through the beam splitter again (see right side figure 4). In this manner, both the astronomical object and the optical fiber tip are imaged on the single CCD. When a probe is located beneath the observing object, images of the astronomical object and the probe coincide on the CCD surface.

The previous optics without the optical cylindrical bar had the problem that the focal points of the probe and the object were incongruent. When the object focuses on the fiber tip, and the viewing optics move into the light path above the probe, the focal length of the object is extended relative to the probe. This property prevented the viewing optics from measuring the positions effectively. The optical cylindrical bar was installed to extend the focal length of the probe. The Newtonian sub mirror obscures the center part of the light from an astronomical object. As the mirror is attached slantingly, the focal ratio of the obstructed light is between F/15.3 and F/21.6. On the other hand, the light from the probe is limited by the diameter of the hole penetrating the electromagnetic manipulator to F/25.6. The optical cylindrical bar is so thin that the light from the telescope is not obscured. Accordingly, both the focal lengths are congruent, and the viewing optics enables us to measure the probe and the object position precisely.

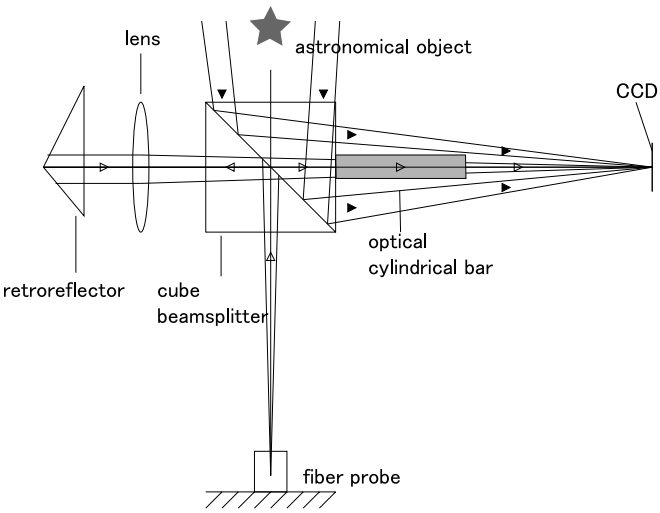

Figure 4. The fiber probe viewing optics. For the reflection plane of the cube beam splitter, the center part is coated as a half mirror. The other part is coated as a total reflection mirror. For the ray from an astronomical object, the part near the light axis is interrupted by sub mirror of the telescope. Filled triangles show the path of the light from an astronomical object and open triangles show the path of the light from the fiber probe. An optical cylindrical bar was added to align the both focal lengths. The details are shown in the text.

2.1.2. *Positional Measurement by the Fiber Probe Viewing Optics*

The beam splitter in the optics is made of two right-angle prisms. One has an aluminized hypotenuse surface, and the other has an uncoated hypotenuse surface. The hypotenuse surfaces of the both prisms were glued together, and the beam splitter was constructed. We examined whether the beam splitter surfaces facing each other were parallel. This parallelism influences position measuring accuracy. When the light reflected by the retro reflector passes through the beam splitter which has no parallel surfaces, the axis of the light from the probe bends. In contrast, the light from an astronomical object is not influenced by this at all. We found that the fiber probes are allocated at incorrect positions, therefore the amount of light that enters the probe decreases.

Figure 5 shows the schema of the experiment. The collimated light is intercepted by a screen with two holes in order to divide the light into two rays. The bottom ray passes through the beam splitter, and the top ray runs straight. Both rays are focused by a convex lens. When the opposite surfaces of the beam splitter are parallel, two beams are imaged onto the same position.

Figure 6 shows the result of the experiment. Both light images are at the different positions. This means that the opposite surfaces of the beam splitter are not parallel. Therefore, we could not accurately measure the probe position, and so the probes were not placed correctly.

To solve this problem, the most appropriate method is to make the beam splitter with an exact parallel surface and a special aluminized layer. Since this method is quite difficult, we adopted another method. Actually, both lights from the telescope and the fiber probe always pass the same positions of all the optics when the probe is located beneath the object image. Furthermore, the optical parameters such as focal length do not change at all. It means that the positional difference of both images on the CCD is stable. We located the fiber probe at the right position using the offset of the optics. This method allowed the fiber probes to receive light from the telescope correctly.

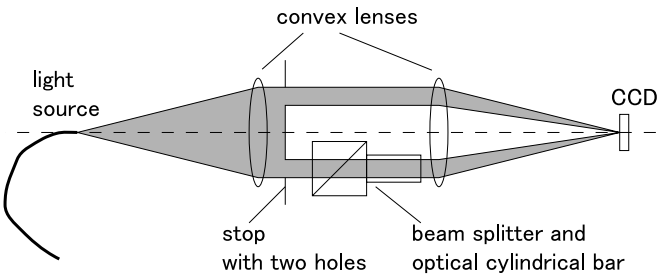

Figure 5. The schema of the experiment to check parallelism of the beam splitter in the fiber probe viewing optics. When the opposite surfaces of the beam splitter are parallel, two rays are imaged on the same position.

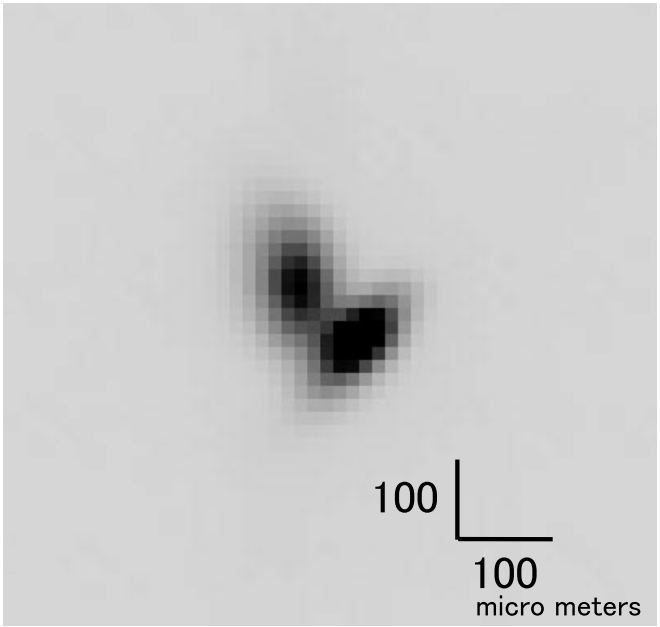

Figure6. The CCD image of the experiment shown in figure 5. One is the image by the ray passing through the beam splitter and the other is by the ray passing through nothing.

2.1.3. *Focusing Position of the Spectral Fiber Probes*

There are two kinds of fiber probes on the focal surface plate: one kind to obtain spectra of astronomical objects and another to monitor a telescope tracking error. The monitoring fibers are image bundle fibers, and we use them for focus checking of the telescope. Both the fiber probes have a tiny right angle prism built-in to lead the light to the fiber. We regularly examine whether the focusing position of monitoring and the spectral fiber probes are consistent.

Each fiber probe was mounted on the optical stage which enabled movement along in the direction of focus. We fed the convergent light into the fibers. The experiment showed a focal discrepancy of 1.65 mm between the two fibers.

The monitoring fiber probes were recomposed. They were evaluated in the same way, and we confirmed that the two kinds of fiber probes had a consistent focus position.

2.2. Instrument Control

2.2.1. *Allocation of Fiber Probes*

The tip of the optical fiber is installed in a metallic case which is called a fiber probe. The probe is picked up by an electromagnetic manipulator and is placed at a predetermined destination on the focal plane. At the end of this sequence, we found two problems when moving the fiber probe to the destination.

When a fiber probe is not placed on a line through the center of the focal plane and the home position of a fiber probe, then the optical fiber is bent and has stress. In order to release the stress, the manipulator head can rotate around the optical axis of the telescope. A ball bearing is built in the manipulator and permits the rotation. However, the stress was insufficient to rotate the manipulator head in many cases. The stress was not released until the probe was detached from the manipulator head. This stress caused the probe to move to an incorrect position. This was the one of the reasons for the displacement.

The other problem was a concern about the residual magnetization of the electromagnetic manipulator. Residual magnetization pulled the probe up and placed it out of position as the manipulator detached. The manipulator generated the residual magnetization when the electric current was applied to the electromagnet for a relatively long time. This corresponded to cases when the manipulator carried the probe from a home position to a destination.

These problems were fixed by the way in which the manipulator adjusts the probe position iteratively. A flow-chart is shown in figure 7. At first, the viewing optics measures the position of an astronomical object (1). The optics is installed to the manipulator. The manipulator picks up a fiber probe and locates it at the destination (2). The viewing optics measures the probe position after the manipulator head released it (3). The bending stress of the fiber is released at this step, if it exists. As a result of calculating the probe position error (4), in cases when error is not permissible (5), the manipulator rearranges the fiber probe until it falls within the permissible zone (6). The sequence progresses automatically.

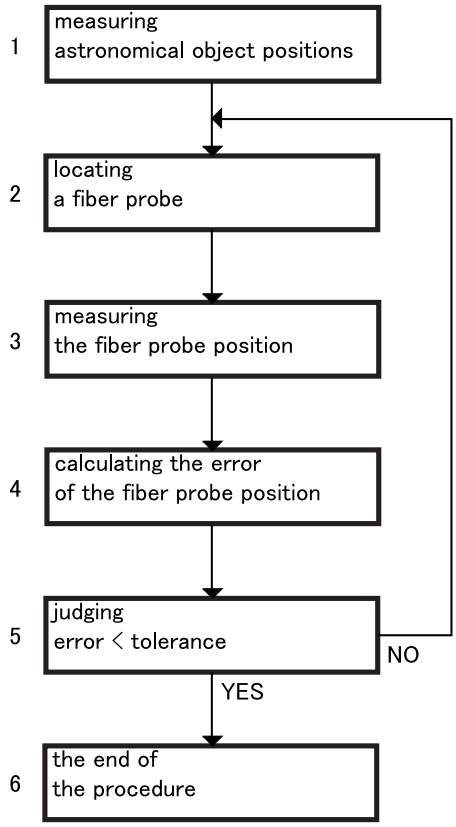

Figure 7. The flow diagram of the arrangement procedure of a fiber probe.

We confirm the result of the sequence in figure 8. The left panel shows the displacement from the destination of fiber probes before the relocation process. Since the diameter of optical fiber core is 113μm, we see the displacement is not negligible. The right panel of figure 8 shows the probe position after the relocation process. We see that the displacement was dramatically reduced; the average error has become 20.7μm from 172.0μm.

We evaluated the effect of the correction of the fiber probe position by experiment. The fiber probe was set on the optical stage which allows it to move everywhere on the focal plane. We fed the convergent light to the fibers. The light has a focal ratio of F/5 and a spot size of 100*μm*. These parameters were set as the Newtonian focus of the telescope. A light power meter measured outgoing power at the other fiber end. The results showed that the throughput for the previous error (172.0μm) and the present error (20.7μm) were 3% and 97%, respectively, when the throughput for the exact position was 100%.

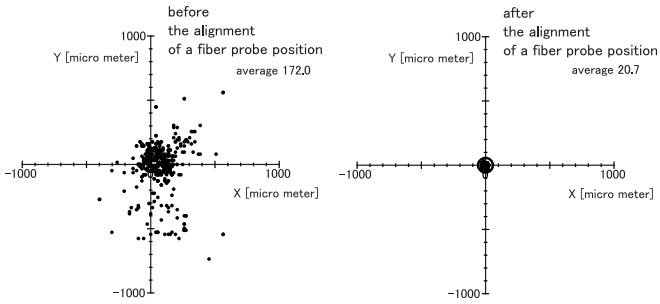

Figure 8. The left panel shows the location accuracy before the relocation procedure of the fiber probe. The right panel shows the location accuracy after the procedure. The center circles show the diameter of the optical fiber core (113μm).

2.2.2. *System and Computers*

The previous instrumental control system forced observers to go through a complicated sequence to arrange fiber probes. The main reason of this was that the CCD of the viewing optics was operated by an independent computer and along with a naive ready-made software. As a result, the positional data of an astronomical object and a fiber probe measured by the viewing optics were manually sent to the system operating the manipulator. This pre-operation reduced total observational efficiency. The refurbished control system fixed the problem. Also, it allowed observers to allocate fiber probes automatically as shown in the previous section.

Two computers (PC1 and PC2) operate in the whole instrumental system as figure 3 shows. PC1 controls all of the instrumental parts except the CCD in the spectrograph. The CCD is operated by a workstation. PC2 is in charge of the Graphic-User-Interface (GUI). Both computers are connected with Ethernet and exchange data in NetBIOS protocol. PC2 receives an order from an observer and issues a command to PC1. PC1 simply operates the instrumental parts and feeds back status information to PC2. PC2 sequentially sends commands to PC1 as it confirms the status information from PC1. All of the instrumental operations are dealt with exclusively by PC1.

Three interface boards slotted into PC1 control the hardware. These are the stage controller board, the RS232C board and the parallel I/O (PIO) board. The stage controller board operates the XYZ stage installed in the manipulator which carries fiber probes. The RS232C board controls the CCD (SBIG ST4) which measures the positions of fiber probes and astronomical objects. The PIO board switches four items on and off. These are the electromagnet which holds fiber probes, the motor moving the mid-field camera, the solenoid fixing bundle fiber probes and the comparison lamp.

PC2 holds the hardware status and the positions of all fiber probes and observed astronomical objects. PC2 receives an image of a fiber probe and an astronomical object acquired by the viewing optics via PC1. Subsequently, PC2 detects the position by a threshold method. Some automatic sequential operation commands as figure 7 shows are programmed by PC2.

GUI consists of two windows (GUI1 and GUI2). The bottom left window is GUI1 and the top right window is GUI2 in figure 9. GUI1 is used for instrument operations and shows the image of the fiber probe and/or astronomical object obtained by the viewing optics. GUI2 takes charge of the confirmation of a fiber probe configuration. Observers operate the instrument using the menu shown above left in figure 9.

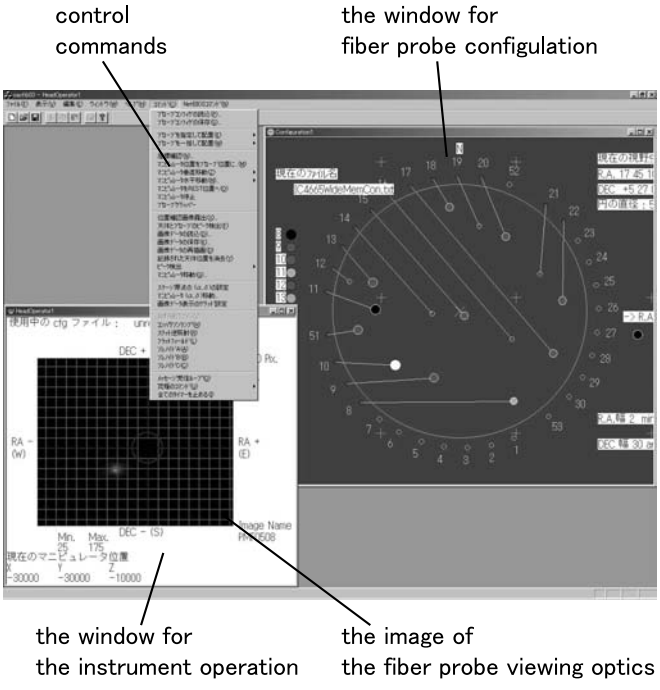

Figure 9. The user interface of OFMS.

2.3. Spectrograph

We have exchanged the Okayama Cassegrain Spectrograph for a CP200 which was manufactured by Jobin Yvon. A concave grating is included in this spectrograph. The output beam of an optical fiber has maximum intensity at the center. As the spectrograph has a structure in which the central portion of the incident beam is not obstructed, then this spectrograph is suitable for fiber spectroscopy. The resolution is $\lambda/\Delta\lambda = 100 - 150$. The 1KCCD at Kiso Observatory is used as the detector which includes a TC215 developed by Texas Instruments. The detector is operated by a workstation computer.

Measuring the fiber probe positions with the viewing optics, the fibers are illuminated by a high-luminance LED. This mechanism is installed next to the slit composed of the fibers and is operated by PC1.

3. Performance

The relocation method has raised the precision of fiber allocation. The results were shown in section 2.2.1. The average accuracy is 21μm. An experiment showed that the light power received at the position of 21μm from the correct position was estimated at 97% of the throughput at the correct position.

The automatic fiber allocation system shortened the amount of time before an observation. It takes about 3 minutes per fiber and about 90 minutes for 30 fiber probes at the maximum. Similarly, it reduced the work of observers to arrange the fiber probes.

Table 1 shows the results of the developments.

Table 1. Performances.

	1994	1998
Instrumental Functions and Operations	Foundation	Completion
Fiber Allocation Accuracy (fiber core size : 113μm)	~170μm	21μm
Observation Efficiency	30 min., S/N 3 for galaxy (V_T=11)	0.6 min., S/N 100 about star (mv=10)
Fiber Allocation Time [/field /30 fibers]	4 hours	1.5 hours
Fiber Position Alignment	manual adjustment	automatic reallocation
Total Number of Observing Objects [/night (8 hours)]	60	150

4. Observation

Galactic abundance gradients of have been the subject of a considerable number of studies over the past decade. In 1993, Friel and Janes showed the metallicity gradient of

$$\Delta[\mathrm{Fe/H}]/\mathrm{R_{gc}} = -0.095 \pm 0.017 \mathrm{dex/kpc}$$

for 33 clusters (where R_{gc} is Galactocentric distance). Twarog, Ashman and Anthony-Twargo (1997) reported a slightly different value of –0.07dex/kpc for 76 clusters. However, a large number of studies on the [Fe/H] gradient of the Galaxy revealed that the dispersion of [Fe/H] for the same distance group of open clusters was significantly larger than the observational error. It is a mystery why such a large difference exists in the [Fe/H] distribution. Our study focuses attention on the dispersion of [Fe/H]. We selected clusters which have similar characteristics for the study. To reduce the confusion of the age-metallicity effect, we selected the clusters which belong to the same age group (<1Gyr). Furthermore, to reduce the spatial variations of [Fe/H], the clusters within 1kpc of the Sun were chosen.

This study requires multiple spectra of each star in the cluster. The size of the cluster is about a few tens of arc-minutes. Since the OFMS has a FOV of 1 degree and is capable of obtaining 30 spectra at the maximum, it is most suitable for our study. From 30th of April to 6th of May in 1999, we observed 4 open clusters and 16 stars for the [Fe/H] calibration at the Okayama Astrophysical Observatory (OAO) by using the OFMS attached to the Newtonian focus in the OAO 1.8m telescope.

Figure 10 is the observational configuration of fiber probes on top of a DSS image of IC4665. In this configuration, we arranged 10 fiber probes at target star positions and 6 fiber probes at blank sky. The data of the 6 fiber probes was used for the reduction. Figure 11 shows the raw image of the spectra. We confirm 10 star spectra in this figure. The analyzed spectra are plotted in figure 12.

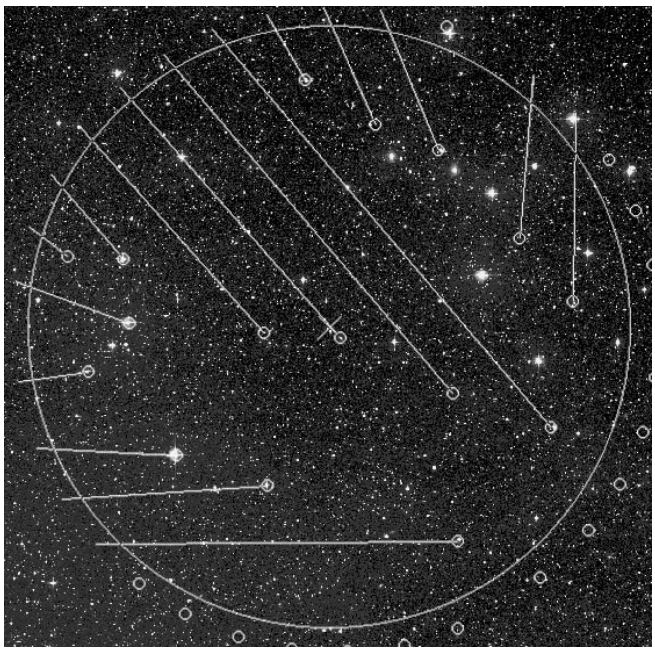

Figure 10. The observational configuration of fiber probes shown on top of a DSS image of IC4665.

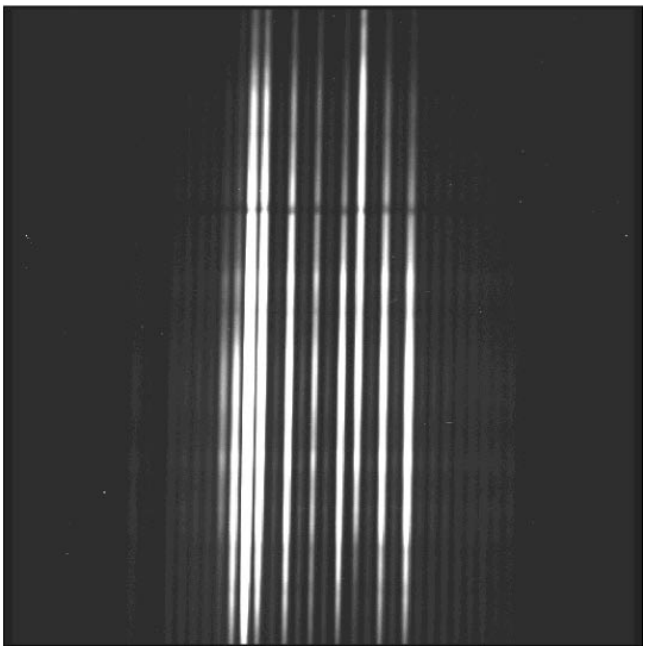

Figure 11. The raw spectra image of IC4665. Thirty apertures of the fibers line up horizontally and each spectrum is observed vertically. Above dark horizontal line shows the absorption by A-band.

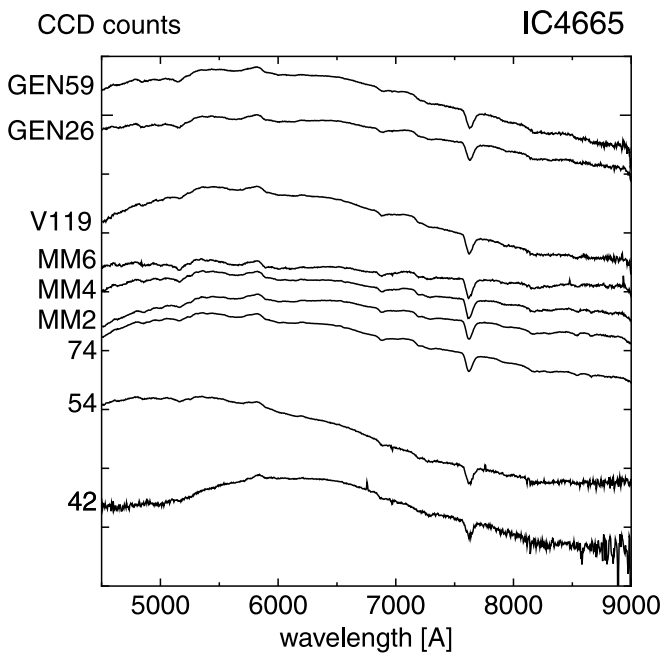

Figure 12. The spectra of IC4665. Values of the y-axis are not absolute. Each spectrum is shifted vertically to avoid crossing.

4.1. [Fe/H] Measuring Method

We adopted the metallicity index method presented by Friel (1987) (FR87) to measure [Fe/H]. She defined 15 spectroscopic metallicity indices. The index is the ratio of the average flux near the center of the feature to the average continuum flux. The index is expressed as a magnitude. The continuum flux is defined as the average of the fluxes on both sides of the feature. As an illustration of the indices, the Fe4680 index is shown as

$$\mathrm{Fe}_{4680} = -2.5 \log \frac{\int_{4636}^{4723} \mathrm{F}_\lambda \, \mathrm{d}\lambda / 87\,\text{Å}}{\int_{4606}^{4636} \mathrm{F}_\lambda \, \mathrm{d}\lambda / 30\,\text{Å} \;+\; \int_{4736}^{4773} \mathrm{F}_\lambda \, \mathrm{d}\lambda / 37\,\text{Å}}.$$

Comparing these indices with [Fe/H] determined by the precise spectroscopic study, she investigated the relation between the indices and [Fe/H]. She found that the indices are mainly controlled by the [Fe/H], slightly depending on the stellar color $(B - V)_0$. She drew constant [Fe/H] lines on the index-$(B - V)_0$ plane. Therefore, a pair of index and $(B - V)_0$ will give one estimation of [Fe/H] for a target star. By using suitable weights for each estimation, we could obtain the final estimation of the [Fe/H] for the target star.

The FR87 method requires 11 metallicity indices and assigns various weights to the indices according to any situation. During our observation, we could not adequately measure 8 indices bluer than Fe4680 due to a mechanical problem. For that reason, we evaluated the possibility to simplify the FR87 method. Since three indices Fe4680, Fe4920 and Fe5270 are easy to measure with the OFMS, we focused on them. To optimize the weighting factors among 3 indices, we used the indices for 54 stars shown in the FR87. These stars were selected so as to have the broad [Fe/H] range from –0.75 to + 0.55. The weighting factors we estimated are indicated in table 2. The weighting factor of the Fe4680 index is larger than the other two indices. This result indicates that the Fe4680 index is effective to estimate [Fe/H]. Figure 13 shows the correlation diagram for [Fe/H] which is derived from 3 indices relative to standard values. The rms deviation from the standard [Fe/H] value is 0.16 dex. By comparison with the FR87 result which has an equivalent value of 0.16 dex, we confirm that the 3-indices method is enough to estimate [Fe/H].

Table 2. The weights for [Fe/H] estimates.

criteria	*a*	*b*	*c*
$0.01 \le x_1, -0.5 < x_3$	0.700	0	0.312
$0.01 \le x_1, x_3 \le -0.5$	0.821	0.051	0.128
$x_1 < 0.0, -0.5 < x_3$	0.364	0.062	0.609
$x_1 < 0.0, x_3 \le -0.5$	0.600	0.074	0.196

$y = ax_1 + bx_2 + cx_3$

y :[Fe/H], x_1:$[\mathrm{Fe/H}]_{\mathrm{Fe4680}}$, x_2:$[\mathrm{Fe/H}]_{\mathrm{Fe4920}}$, x_3:$[\mathrm{Fe/H}]_{\mathrm{Fe5270}}$

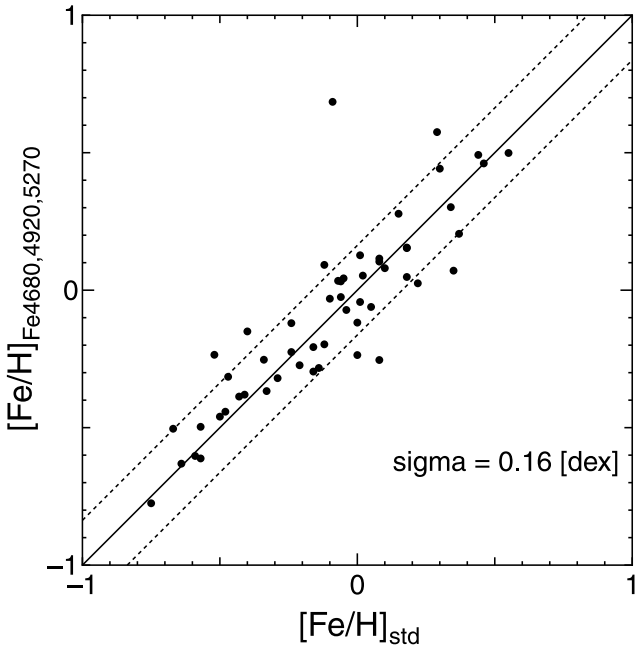

Figure 13. The correlation diagram of [Fe/H] estimated by 3 indices (Fe4680, Fe4920 and Fe5270) relative to standard values. FR87 data are used in the diagram. The rms deviation is 0.16 dex.

4.2. [Fe/H] Calibration Stars

We observed 16 stars for [Fe/H] calibration. The standard [Fe/H] and the metallicity indices in FR87 of these stars were already known. This allows us to check the spectra obtained by our observation in comparison with FR87 indices. Table 3 shows these stars and their characteristics.

We calibrate the indices taken by the OFMS to the FR87 indices. It is proper to calibrate our indices and the color $(B - V)_0$ to the standard [Fe/H], however we have not obtained enough data to do it as yet. Therefore, we transform our indices to the FR87 indices and estimate [Fe/H] by using the transformed indices and the color-index diagram indicated in the FR87.

Figure 14 shows the correlation diagram of our Fe4680 index and FR87's. We confirm the good correlation between two indices. It should be noted that we use the unit of CCD counts to derive the index, although the indices of the FR87 were derived from the flux. However, figure 14 indicates that the index we found does not make much difference from the FR87 index. We consider that the error issued by using the CCD counts is regarded as a subset of the total error caused by the transformation from our indices to FR87 indices.

The correlation coefficients between our metallicity indices and those of the FR87 are shown in table 4. These 15 indices are shown in the FR87 and include 12 indices we do not use in this study. For the 8 indices bluer than Fe4680, we could not acquire an adequate number of samples due to a mechanical problem. We find 4 indices accompanied with an asterisk in table 4. According to Friel(1987), these indices do not show a high correlation with [Fe/H]. We confirm that Fe4680, Fe4920, and Fe5270 indices have an adequate correlation coefficient. Table 5 indicates the coefficients of the transforming function from our indices to the FR87 indices. We confirm that the Fe4680 index has a high correlation coefficient (0.92). Previously, we found that the Fe4680 index has a large weighting factor, it is shown in table 2. These results indicate that the Fe4680 index is extremely effective to estimate [Fe/H].

Table 3. Metallicity calibration stars.

ID	*mv*	$(B - V)_0$	[Fe/H]	Sp. Type
HD146470	8.43	1.35	–0.67	K4III
HD134063	7.82	0.92	–0.60	G8III
HD81192	6.54	0.95	–0.57	G8III
HD107328	5.00	1.16	–0.47	K1III
HD117876	6.11	0.96	–0.41	K0III
HD100030	6.42	0.88	–0.29	G8IV
HD92588	6.26	0.88	–0.25	K1IV
HD91612	5.08	0.93	–0.21	G9III
HD112127	6.91	1.27	–0.09	K2III
HD97907	5.32	1.20	–0.05	K3III
HD129312	4.87	1.01	+0.00	G8III
HD108225	5.02	0.95	+0.01	G8III-IV
HD76291	5.74	1.09	+0.08	K1IV
HD104304	5.54	0.76	+0.18	K0IV
HD72324	6.34	1.02	+0.22	G9III
HD125560	4.85	1.23	+0.30	K3III

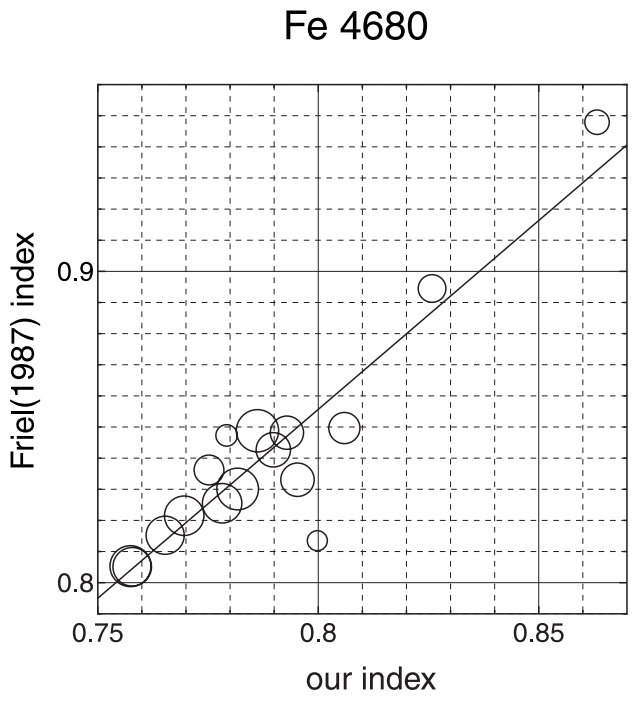

Figure 14. The correlation diagram between FR87 and our metallicity index for Fe4680. The radius of each circle shows the magnitude of error.

Table 4. Correlation coefficients of the metallicity index.

metallicity index	correlation coefficient
Mg3838*	–0.32
CN3883*	0.89
Ca II H+K	0.36
Fe4065	0.78
CN4216	0.05
Ca4226*	0.59
G-Band*	0.75
Fe4530	0.87
Fe4680	0.92
Fe4920	0.51
Fe5011	0.22
Mg	0.93
Fe5270	0.52
Fe5335	0.01
Fe5400	0.20

Table 5. The index transformation function from ours to FR87.

Index	*a*	*b*
Fe4680	1.2135	–0.1151
Fe4920	0.2331	0.5927
Fe5270	0.7859	0.2193

$y = ax + b$

x: our index, *y*: FR87 index.

We find the figures which define the lines indicating a constant [Fe/H] on the diagrams of $(B - V)_0$ and the FR87 indices. The figures for the Fe4680 and the Fe5270 are shown in the FR87, however the relation between the Fe4920 index and [Fe/H] is not indicated. We used the data of standard stars shown in the FR87 and defined the lines indicating the constant [Fe/H] values about the Fe4920 index by the least square method.

In this manner, our indices are transformed to the FR87 indices, and each [Fe/H] for Fe4680, Fe4920 and Fe5270 is estimated. Conclusive [Fe/H] is calculated by a weighted mean of each [Fe/H]. We estimate the error of our method by using the derived [Fe/H] of the calibration stars we observed. Figure 15 shows the correlation diagram for [Fe/H] derived from our data relative to standard value. The rms deviation is 0.26 dex. We use this value as the error caused by our system. In the case of a star cluster, net error is reduced, since the metallicity is derived statistically from each star,

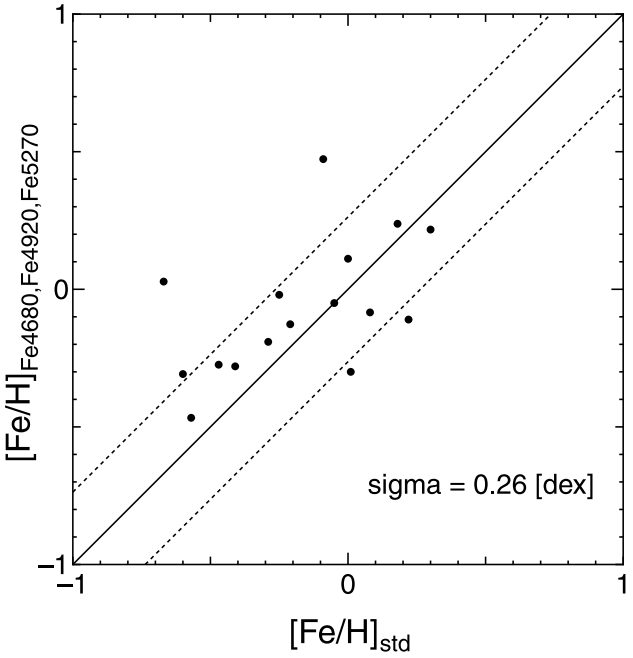

Figure 15. The correlation diagram of [Fe/H] estimated by 3 indices (Fe4680, Fe4920 and Fe5270) relative to standard values. Our data are used in the diagram. The rms deviation is 0.26 dex.

4.3. Open Clusters

We selected four open clusters, NGC6709, IC4655, NGC6866 and NGC6633 as targets. These clusters have the age of less than 1Gyr and distances of less than 1kpc. Our method to estimate [Fe/H] is applied to giants and subgiants (also FR87). Firstly, we made a color-magnitude diagram of each cluster and selected the stars on the red giant branch with the color $(B - V)_0 > 0.5$. A total of 25 stars were found from four clusters. They are shown in table 6.

The NGC6709-HSS208 and IC4665-MM2 spectra appear in figure 16 as examples. Three dark gray zones denote the regions absorbed by metal in the star atmosphere. The regions are Fe4680, Fe4920 and Fe5270 in turn as seen from the left. The regions defined as continuum are indicated by light gray zones on both sides of each dark gray zone. We confirm the absorbed feature on the NGC6709-HSS208 spectrum in the Fe4680 index zone and the shallow feature on IC4665-MM2 spectrum. This trend is also found in the Fe4920 and Fe5270 index zone.

Table 6. Target stars in clusters.

ID	α(2000)	δ(2000)	mv	(B–V)	$(B–V)_0$
NGC6709 HSS208	18 51 32	+10 19 09	9.2	1.55	1.23
NGC6709 HSS303	18 51 10	+10 18 06	9.1	1.31	0.99
IC4665 42	17 45 14	+5 25 58	10.6	1.40	1.24
IC4665 54	17 45 51	+5 43 30	10.4	1.40	1.24
IC4665 74	17 46 41	+5 29 19	10.2	1.50	1.34
IC4665 MM2	17 44 13	+5 15 02	7.8	1.28	1.12
IC4665 MM4	17 44 47	+5 12 13	9.7	1.27	1.11
IC4665 MM6	17 45 01	+5 50 01	10.2	1.29	1.13
IC4665 V119	17 46 33	+5 17 39	10.3	1.27	1.11
IC4665 GEN+3.46650024	17 43 53	+5 33 17	9.3	1.25	1.09
IC4665 GEN+3.46650026	17 43 55	+5 27 23	8.1	1.26	1.10
IC4665 GEN+3.46650059	17 45 58	+5 07 05	11.0	1.39	1.23
NGC6866 5	20 03 55	+44 08 24	11.6	1.00	0.87
NGC6866 26	20 03 34	+44 02 32	9.4	1.50	1.37
NGC6633 41	18 26 23	+6 55 34	9.1	1.20	1.03
NGC6633 42	18 26 24	+6 40 51	10.6	1.80	1.63
NGC6633 121	18 28 20	+6 35 23	10.7	1.23	1.06
NGC6633 124	18 28 22	+6 21 02	10.3	1.50	1.33
NGC6633 HILT14	18 26 33	+6 31 34	8.3	1.06	0.89
NGC6633 HILT56	18 27 05	+6 32 14	8.2	0.82	0.65
NGC6633 HILT67	18 27 14	+7 00 33	7.3	1.43	1.26
NGC6633 HILT116	18 27 54	+6 36 01	8.3	1.09	0.92
NGC6633 HILT122	18 28 00	+6 54 51	8.7	1.07	0.90
NGC6633 HILT140	18 28 22	+6 42 30	8.8	1.04	0.87
NGC6633 SAN456	18 28 17	+6 45 59	9.0	1.01	0.84

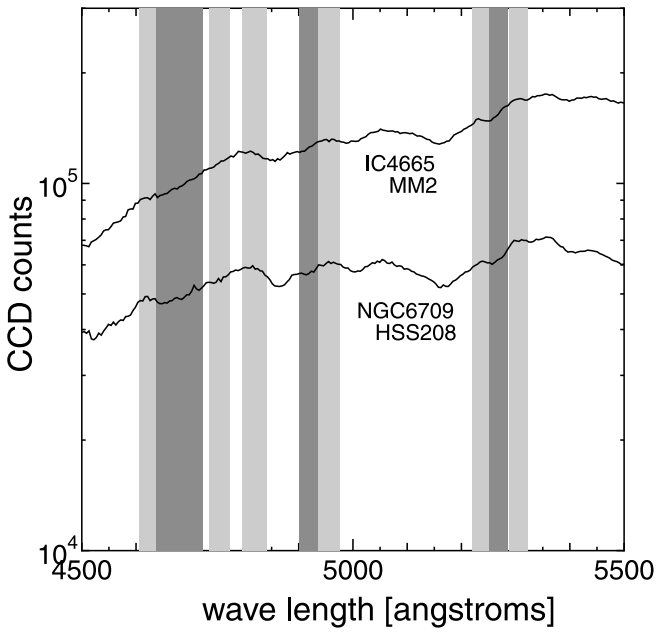

Figure 16. The spectra of IC4665-MM2 and NGC6709-HSS208. Dark gray rectangles and light gray rectangles show the central regions and the continuum regions to measure metallicity indices, respectively. Three regions are Fe4680, Fe4920, Fe5270 from left to right.

We derive the metallicity indices from the spectrum and they are transformed into the FR87 indices with the transformation function. The functions were obtained previously using the stars we used to calibrate metallicity. The transformed indices are plotted on a color-index diagram. FR87 showed the constant [Fe/H] lines on the color-index diagram. We determine the [Fe/H] of the star on the basis of the lines. Figure 17 indicates the color-index (Fe4680) diagram for the stars in IC4665. Transverse lines indicate the position with constant metallicity presented by FR87. We determined [Fe/H] of each star and [Fe/H] of the clusters by averaging the value of the stars. [Fe/H]s of each star are shown in table 7.

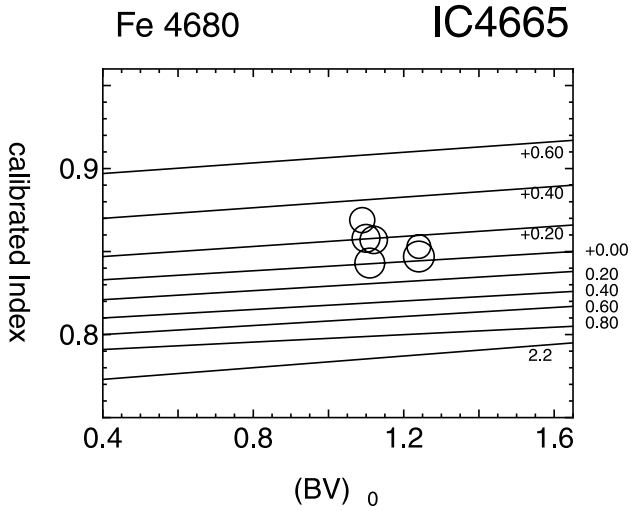

Figure 17. A color-index diagram. Transverse lines indicate the position which has a constant [Fe/H] in FR87. We found the metallicity index Fe4680 for 6 stars of IC4665. The results are shown in the figure. The radius of each circle shows the magnitude of error.

Table 7. [Fe/H] of the cluster member stars.

ID	[Fe/H]	number of observation
NGC6709 HSS208	0.142	1
NGC6709 HSS303	0.162	1
IC4665 42	0.093	2
IC4665 54	0.009	2
IC4665 74	0.113	1
IC4665 MM2	0.142	2
IC4665 MM4	0.005	2
IC4665 V119	-0.095	1
IC4665 GEN+3.46650024	0.296	2
IC4665 GEN+3.46650026	0.111	2
NGC6866 5	-0.738	1
NGC6866 26	0.019	1
NGC6633 42	0.152	1
NGC6633 121	0.001	1
NGC6633 124	0.125	1
NGC6633 HILT14	0.089	1
NGC6633 HILT56	0.029	1
NGC6633 HILT67	0.256	1
NGC6633 HILT116	0.020	1
NGC6633 HILT140	-0.052	1
NGC6633 SAN456	-0.039	1

4.4. Results of the Observation

We determined [Fe/H] of the clusters by averaging the values of the member stars. These values are as follows: +0.15 dex for NGC6709, +0.09 dex for IC4665, –0.36 dex for NGC6866, and +0.07 dex for NGC6633 (table 8). Figure 18-21 shows [Fe/H]s of each member star and cluster. The estimation error is ± 0.26 dex for all clusters. We calculated standard deviations of [Fe/H] for the member stars. These values are as follows: 0.01 dex for NGC6709, 0.12 dex for IC4665, 0.54 dex for NGC6866, and 0.10 dex for NGC6633. These values except NGC6866 are smaller than the error (± 0.26 dex) expected with the calibration stars. We consider two reasons for this. Firstly, member stars of the open cluster are the same age, while the metallicity calibration stars are different ages. If our metallicity indices are affected by the age dependent feature, [Fe/H]s of the member stars of the open cluster distribute with a small variance. However, the metallicities have a systematical error depending on the age. Secondly, for the open clusters, the metallicities of the member stars are measured by the same exposure. For the metallicity calibration stars, metallicity is measured by a number of different exposures. If there is an estimation error by data reduction with respect to each image frame, the metallicities of the clusters are smaller than the error expected with the calibration stars. Consequently, we adopted ± 0.26 dex as the estimation error. In figure 15, there are 2 stars out of touch with the others. It is possible that these 2 stars have unknown characteristics which mean our method cannot estimate the correct [Fe/H] for them. For example, we might have interpreted luminosity class wrongly. When we estimate the error except these stars, the error is reduced to ± 0.18 dex.

In table 7, NGC6866 5 shows extremely poor metallicity compared with the others. We find the strong absorption line by H_β on the spectrum of this star. NGC6866 5 may not be a late type star, but a early type star embedded by interstellar medium.

[Fe/H] of NGC6633 was measured by Piatti et al. (1998), who found [Fe/H] = –0.02 dex. Our result [Fe/H] = +0.07 ± 0.09 dex is consistent with the result within the limits of the error.

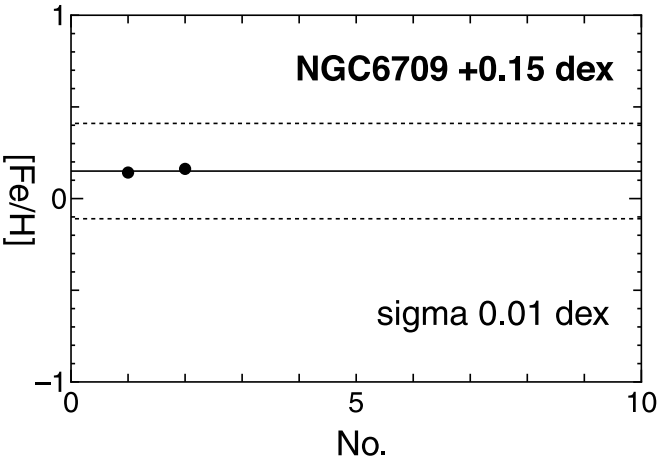

Figure 18. [Fe/H]s of NGC6709 member stars. Dots indicate [Fe/H]s of the star. The average of the metallicities ([Fe/H] of the cluster) is indicated by the line. The dotted lines show the estimation error (±0.26dex). The standard deviation of metallicities of the member star are shown as "sigma".

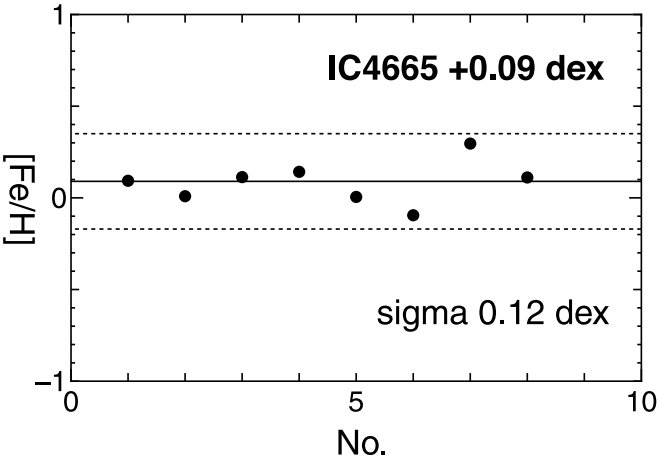

Figure 19. [Fe/H]s of IC4665 member stars.

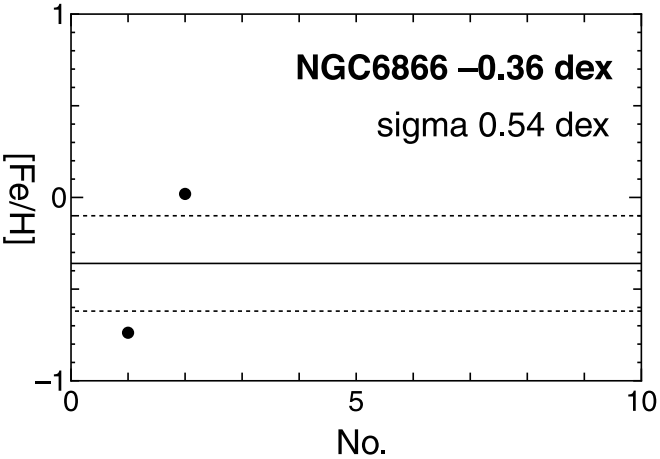

Figure 20. [Fe/H]s of NGC6866 member stars.

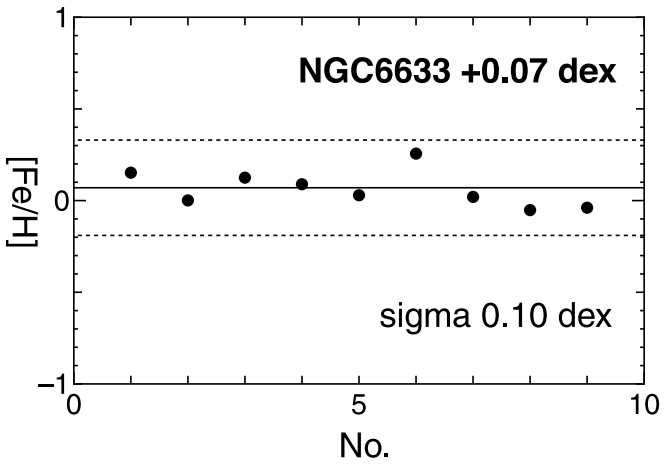

Figure 21. [Fe/H]s of NGC6633 member stars.

Table 8. Metallicty of open clusters.

Metallicity unknown		Metallicity known	
NGC6709(2)	+0.15 dex	NGC6633(9)	+0.07 dex
IC4665(8)	+0.09 dex		
NGC6866(2)	-0.36 dex		

NOTE.–The estimation errors are ± 0.26 dex.

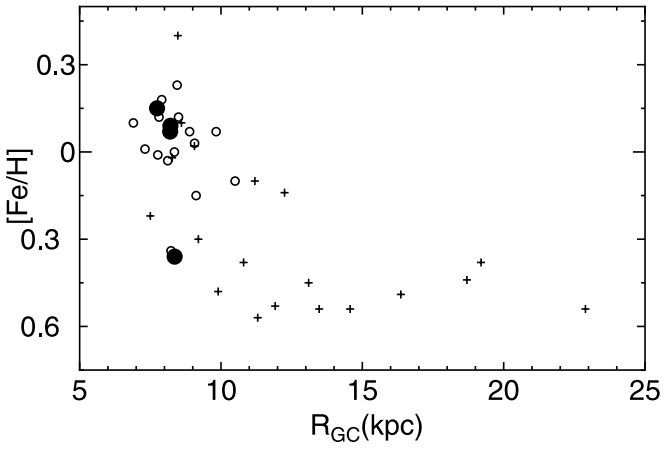

Figure 22. [Fe/H] vs. Galactocentric distance. The filled circles represent the cluster [Fe/H] derived in this study. The open circles and cross signs represent the cluster [Fe/H] taken from the literature, which have the age of <1Gyr and >1Gyr, respectively.

Figure 22 shows [Fe/H] of open clusters relative to galactocentric distance. All plotted clusters are younger than 1 Gyr. We calculated the galactocentric distance of the clusters with the Sun at the position of 8.5kpc. The clusters we measured are indicated as black filled circles. Except for NGC6866 (estimated at –0.36), the iron abundances we measured are consistent enough with other data. Three clusters except for NGC6866 may show that the dispersion of the metallicity gradient is small, although there is not enough data to determine this.

We did not use the Mg index, when we obtained cluster [Fe/H]. However, according to the FR87, it is available to calculate [Fe/H] from the Mg index. It is known that [Fe/H] given by the Mg index is less than [Fe/H] given by Fe indices (Friel and Janes (1993)). This trend is correlated with cluster age and is strongly found for young clusters. For the clusters whose age is about 1Gyr, the difference is about 0.5 dex. For NGC6709, IC4665, NGC6866 and NGC6633, the cluster [Fe/H] calculated from the Mg index were –0.217, –0.486, –0.829 and –0.357, respectively. Our data follow the trend and is consistent with the difference shown by previous study.

5. Summary

The fiber multi-object spectrograph for the Okayama 188cm telescope (OFMS) has been completed by the refurbishment started in 1993. To place the fiber probes precisely to the positions of target objects, we investigated the optics and the mechanics of OFMS. We found four serious problems, (*i*) defocusing of the optics to detect fiber probes, (*ii*) the position error for measuring a fiber probe by the optics, (*iii*) the design error of the fiber probes to adjust telescope focus and (*iv*) unexpected behavior of optical fibers and the electromagnetic manipulator. Problems (*i*) and (*iii*) were fixed by reforming the optics. Problem (*ii*) was fixed by changing the method to use the optics. Problem (*iv*) was fixed by devising the method to place a fiber probe. The manipulator iterates to adjust the position of a fiber probe till it is placed on the precise position. To implement the process automatically, the system controlling OFMS was rebuilt. There are two computers (PC1 and PC2) in the new system. All devices except for the CCD camera of the spectrograph are controlled by PC1. PC1 gathers the status of all devices and directs them. It allows us to construct and execute complicated commands such as adjusting the position of a fiber probe. PC2 has the interface for observers. PC2 sends commands to control the OFMS to PC1 and receives the results. The computer operating the CCD camera of the spectrograph is controlled by PC2. The new system allowed us to place the fiber probe automatically with a precision of less than 20μm. Consequently, the flux of the spectra detected by the OFMS has been increased and it has been enabled to observe a point source object like a star. Additionally, the operation of the OFMS was simplified and the efficiency of observation was improved.

We measured the metallicity abundance [Fe/H] of open clusters by using the completed OFMS. The observed clus-

ters were NGC6709, IC4665, NGC6866 and NGC6633. Additionally, we observed 16 stars for the metallicty calibration. We calculated 3 metallicity indices, Fe4680, Fe4920 and Fe5270 from the spectra and estimated [Fe/H] from the indices. [Fe/H] of NGC6709, IC4665, NGC6866 and NGC6633 was found as $+0.15 \pm 0.01$ dex, $+0.09 \pm 0.12$ dex, -0.36 ± 0.54 dex, and $+0.07 \pm 0.10$ dex, respectively. We calculated the galactocentric distance of these clusters and plotted the data on the figure of [Fe/H] vs. galactocentric distance. Our results are consistent enough with other values taken from the literature. Additionally, our results suggest the possibility that the dispersion of the metallicity gradient is small.

We wish to express our gratitude to Okayama Astrophysical Observatory for providing us with the opportunity for development and observation. We also wish to thank Advanced Technology Center of NAOJ.

References

Bingham, Richard G., et al., 1994, *SPIE,* **2198**, 56.

Bucciarelli B., et al., 1992, *AJ,* **103**, 1689.

Carraro, G., Ng, Yuen Keong and Portinari, L., 1998, *MNRAS,* **296**, 1045.

Claria, Juan J., Piatti, Andres E. and Osborn, Wayne, 1996, *PASP,* **108**, 672.

Edvardson, et al., 1993, *A&A,* **275**, 101.

Friel, Eileen D., 1987, *AJ,* **93**, 1388.

Friel, E. D. and Janes, K. A., 1993, *A&A,* **267**, 75.

Friel, E. D., 1995, *ARA&A,* **33**, 381.

Gray, M. Peter, 1986, *SPIE*, **627**, 96.

Heacox, William D., 1986, *AJ*, **92**, 219.

Henry, R. B. C., et al., 1992, *MNRAS,* **258**, 321.

Hill, John M., et al., 1980, *ApJL,* **242**, L69.

Hill, John M., 1988, *A.S.P. Conf. Ser*., **3**. 77.

Hoag A. A., et al., 1961, *Publ. U.S. Naval Obs. Second Serie*, **17**, 343.

Jacoby, G. H., Hunter, D. A. and Christian, C. A., 1984, *ApJS,* **56**, 257.

Janes, K. A., 1979, *ApJS,* **19**, 135.

Janes, K. A., 1988, In *Calibration of Stellar ages*, Editor, A. G. Davis Philip, Publisher, L. Davis Press, Schenectady, N.Y , 59.

Landolt, Arlo U., 1992, *AJ,* **104**, 340.

Lewis, Ian J., Jones, Lewis R. and Parry, Ian R., 1994, *SPIE,* **2198**, 947.

Lyngå, G., 1987, *Catalogue of Open Cluster Data* (Strasbourg: Center de Donnees Stellaires).

Massey, P., et al., 1988, *ApJ,* **328**, 315.

Matteucci, F. and François, P., 1989, *MNRAS,* **239**, 885.

McWilliam, Andrew, 1997, *ARA &A,* **35**, 503.

Mito, H., 2000, Doctoral Thesis, Department of Astronomical Science, The Graduate University for Advanced Studies.

Noumaru, J., et al., 1993, *Publ. Natl. Astron. Obs. Japan,* **3**, 107.

Parry, Ian R. and Gray, Peter M., 1986, *SPIE,* **627**, 118.

Parry, Ian R. and Lewis, Ian J., 1990, *SPIE*, **1235**, 681.

Parry, Ian R., et al., 1993, *A.S.P. Conf. Ser*., **37**, 36.

Parry, Ian R., et al., 1994, *SPIE,* **2198**, 125.

Parry, Ian R., 1998, *A.S.P. Conf. Ser*., **152**, 3.

Piatti, Andres E., Claria, Juan J. and Abadi, Mario G., 1995, *AJ,* **110**, 2813.

Piatti, Andrés E., Clariá, Juan J. and Bica, Eduardo, 1998, *ApJS,* **116**, 263.

Ramsey, Lawrence W., 1988, *A.S.P. Conf. Ser.,* **3**, 26.

Rolleston, W. R. J., et al., 2000, *A&A,* **363**, 537.

Smartt, Stephen J. and Rolleston, William Robert J., 1997, *ApJL,* **481**, 47.

Thogersen, E. N., Friel, E. D. and Fallon, B. V., 1993, *PASP,* **105**, 1253.

Twarog, Bruce A., Ashman, Keith M. and Anthony-Twarog, Barbara J., 1997, *AJ,* **114**, 2556.

Watson, F. G., 1995, *A.S.P. Conf. Ser*., **84**, 71.

Worswick, Susan P. et al., 1994, *SPIE,* **2198**, 44.

Yong, David, Carney, Bruce W. and Teixera de Almeida, Maria Luísa, 2005, *AJ*, **130**, 597.